

Influence of silver-nanoparticle layer in a chiral sculptured thin film for surface-multiplasmonic sensing of analytes in aqueous solution

Stephen E. Swiontek* and Akhlesh Lakhtakia

The Pennsylvania State University, Department of Engineering Science and Mechanics,
NanoMM—Nanoengineered Metamaterials Group, 212 EES Building,
University Park, PA 16802, USA

*ses1034@psu.edu

Abstract. Multiple surface-plasmon-polariton (SPP) waves at a single free-space wavelength can be guided by the interface of a metal and a chiral sculptured thin film (STF). Multilayers comprising a chiral STF of lanthanum fluoride deposited on an aluminum thin film deposited on a glass substrate were fabricated. In some chips, a 5-nm-thick layer of silver nanoparticles was deposited at [one of two selected depths in](#) the chiral STF. The chips were then deployed in a prism-coupled configuration in a custom-built machine for surface multiplasmonic resonance imaging (SMPRI), in order to observe the effects the silver-nanoparticle layer on the multiple SPP-wave modes. The angular locations of the SPP-wave modes were found to be not greatly dependent on whether the silver-nanoparticle layer was deposited after the first or the second period of a three-periods-thick chiral STF. With aqueous solutions of sucrose as infiltrant fluids, the angular shifts of the SPP-wave modes were determined as the refractive index of the infiltrant fluid increased. The use of a [charge-coupled devices \(CCD\)](#) camera and upgraded motion-control equipment for SMPRI was found to increase the sensitivity of the chip. The silver-nanoparticle layer was also found to enhance the sensitivity.

Keywords: chiral sculptured thin film, optical sensing, surface multiplasmonics, surface-plasmon-polariton wave

1 INTRODUCTION

1.1 Surface-plasmon-polariton waves

The surface plasmon-polariton (SPP) wave has dominated research on electromagnetic surface waves for several decades due to the simple and easy way of exciting it in academic, research, and industrial settings for optical-sensing purposes [1]. To date, the SPP-wave phenomenon has been exploited to sense hundreds of biological, chemical, and biochemical analytes with high sensitivity [2–7].

In most practical implementations, the SPP wave is guided by the interface of a thin metal film and an isotropic dielectric material, with both materials taken to isotropic and homogeneous [1, 4]. An associated drawback is that only *one* SPP-wave mode can be guided by the metal/dielectric interface at a specific free-space wavelength when the dielectric material is homogeneous [8–11]. However, understanding of the SPP-wave phenomenon has evolved to encompass partnering dielectric materials that are periodically nonhomogeneous in the direction normal to the interface. Chiral liquid crystals [12] and periodically nonhomogeneous sculptured thin films (STFs) [13] exemplify such dielectric materials. The interfaces of these dielectric materials with metals have been experimentally shown to be able to guide *multiple* SPP-wave modes at a single free-space wavelength [14–16]. This development has engendered the field of *surface multiplasmonics* [11] and has led to *surface-multiplasmonic sensing* of single analytes [17, 18].

The Turbadar–Kretschmann–Raether (TKR) configuration [8, 10, 11] illustrated in Fig. 1 is the most common method to excite an SPP wave, as its implementation is inexpensive. In this configuration, a thin film of a plasmonic metal—such as aluminum—is deposited through a physical-vapor-deposition (PVD) technique onto the hypotenuse of a 45° - 90° - 45° prism of refractive index n_{prism} which is sufficiently high. Suppose that air, which is an isotropic dielectric material with refractive index $n_{air} = 1$, partners that metal thin film. Both materials are isotropic and homogeneous. A monochromatic p -polarized plane wave of fixed intensity is directed towards one slanted surface of the prism at an angle α shown in Fig. 1. After refraction, light is incident on the prism/metal interface at an angle θ with respect to the normal to that interface, where

$$\sin(\alpha - \pi/4) = n_{prism} \sin(\theta - \pi/4). \quad (1)$$

Light is then reflected from the prism/metal interface towards the other slanted face. On emergence from that slanted face, the intensity of light is measured, typically with a photodetector. On a plot of the measured reflectance against θ , a sharp drop in reflectance is seen. This drop in reflectance is indicative of the excitation of an SPP wave guided by the interface of the two partnering materials, provided the transmittance through the metal film into air is null valued. If air is replaced as the partner of the metal film by some other isotropic dielectric material such as an aqueous solution, the value of θ for the reflectance drop changes. Thus, the angular location of the SPP wave can be used to determine the refractive index of the partnering dielectric material. This technique allows a single SPP wave to sense the presence of an analyte infiltrating the partnering dielectric material. The principle remains the same even if the partnering dielectric material were to be anisotropic [11].

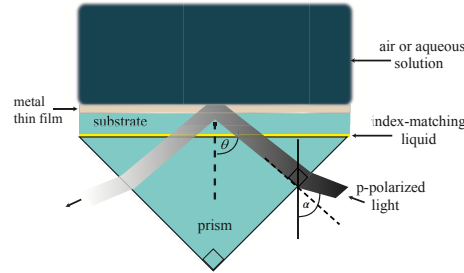


Fig. 1. Schematic of the TKR configuration for optical sensing. A substrate with a metal thin film is affixed to the hypotenuse of a 45° - 90° - 45° prism. Ideally, the substrate and the prism have the same refractive index. On the other side of the metal film is an aqueous solution (or some other fluid) containing the analyte to be sensed. A monochromatic p -polarized plane wave is incident onto one slanted face of the prism and emerges from the other slanted face of the prism.

However, if the partnering dielectric material were to be periodically nonhomogeneous in the thickness direction, *multiple* SPP-wave modes may be guided at a single wavelength. If that dielectric material were to be porous as well, *multiple* analytes could possibly be sensed at the same time [17]. A chiral STF meets these requirements [18].

1.2 Chiral sculptured thin films

A chiral STF is a periodically nonhomogeneous material comprising parallel nanohelices oriented along the thickness direction [13]. The material is grown on planar substrates through PVD techniques in a low-pressure chamber. The morphology is developed by tilting the substrate so that a collimated flux of an evaporated material is directed towards the substrate at an angle $\chi_v \in (0^\circ, 90^\circ]$ with respect to the substrate plane. After χ_v is fixed, at a fixed rate the

substrate is rotated about an axis which passes normally through it while deposition is taking place [11].

1.3 Surface multiplasmonic resonance imaging (SMPRI)

In the traditional TKR configuration, a photodetector is used to measure the intensity of light emerging from the second slanted face of the prism. If the photodetector is replaced by a [charge-coupled devices \(CCD\)](#) camera, the technique is called surface plasmon-resonance imaging (SPRI) [19, 20]. This label-free technique is used to monitor protein-carbohydrate interactions, immunoassays, and bioaffinity interactions [21–23].

The hallmark of SPRI is that nanoparticles of either gold or silver can be functionalized to attach recognition molecules which will attract analytes of a certain kind [24]. These functionalized nanoparticles can be sensed through [SPRI](#), as it is very sensitive to minute changes in the proximity of the substrate/thin-film environment [25]. Also, functionalization makes SPRI very selective.

This very-sensitive SPRI has the potential to sense multiple analytes or interactions at the same time in the surface-multiplasmonics scenario, leading thereby to surface-*multiplasmonic*-resonance imaging (SMPRI). If a silver-nanoparticle layer can be embedded within a chiral STF, it is possible that the silver nanoparticles can be functionalized with specific recognition molecules to attach to specific analytes. Abbas *et al.* have shown that the dynamic sensitivity of the sensor itself can increase [dramatically](#), provided that the volume fraction of silver nanoparticles embedded throughout a chiral STF does not exceed 1% [26].

Moving towards eventually a practical implementation of SMPRI for multi-analyte sensing, we decided to fabricate chiral STFs containing thin layers of silver nanoparticles [27]. But as the effects of silver-nanoparticle layers on surface multiplasmonics and optical sensing of analytes were not known within an experimental setting, we undertook the research reported here.

The plan of this paper is as follows. Section 2 provides detailed descriptions of (a) the fabrication process of all samples used in this work and (b) an explanation of the reflectance-measurement process. Experimental results are presented and discussed in Sec. 3. Chief conclusions are succinctly delineated in Sec. 4.

2 MATERIALS AND METHODS

In order to implement the TKR configuration for SMPRI, we selected both the prism and the substrate to be made of SF11 glass and the chiral STF to be made by evaporating lanthanum fluoride (LaF_3). Aluminum (Al) was selected for the metal film, and silver (Ag) for the nanoparticles. The layer of silver nanoparticles must be thin enough so that it does not drastically change the optical response of the sensor and it must also provide a sufficiently large density of binding sites for recognition molecules and analytes. After several experimental and simulation studies [17], the thickness of the silver-nanoparticle layer was fixed at 5 nm.

2.1 Fabrication of SMPRI chips

Each SMPRI chip comprises a SF11 glass substrate on one face of which a dense thin film of Al and a chiral STF of LaF_3 are deposited. The chiral STF may or may not contain a layer of Ag nanoparticles.

2.1.1 Deposition of Al thin film

The thin-film-deposition process begins with a thorough cleaning of $3.56 \times 3.56\text{-cm}^2$ SF11 glass substrates (Swiss Jewel, Philadelphia, PA, USA) of refractive index $n_{\text{SF11}} = 1.778$. The substrates were cleaned in an ultrasonic bath after the mechanical cleaning and blow dried with a nitrogen gun. Then, four substrates were mounted onto a rotatable sample holder with Kapton[®] tape (Uline, Pleasant Prairie, WI, USA) for simultaneous deposition of Al thin films.

A custom-built low-pressure chamber was prepared to hold a tungsten-wire basket (B1-.040W, R.D. Mathis, Long Beach, CA, USA) which housed an Al pellet. A deposition controller was programmed to accommodate three material-specific parameters (bulk density, z -ratio, and tooling factor) for Al. The sample holder was then placed in the chamber and oriented to ensure that $\chi_v = 90^\circ$ [28]. In order to facilitate the deposition of a planar, dense, and homogeneous thin film, a computer-controlled stepper motor was turned on to rotate the sample holder at 120 rpm about a central normal axis passing through the sample holder. A shutter between the basket and the sample holder was then engaged to block any vapor flux from reaching the substrates, the door of the chamber was then closed, and air was evacuated from the chamber until a base pressure $P_{\text{base}} = 10^{-6}$ Torr was reached.

Electrical current was then passed through the tungsten-wire basket to heat the Al pellet. The current was slowly increased. Aluminum began to sublime when the current was approximately 32 A. The shutter was disengaged and a quartz crystal monitor (QCM) mounted close to the samples was used to maintain a deposition rate of 0.1 nm s^{-1} . Once the QCM had indicated that a 30-nm-thick Al film had been deposited, the shutter was re-engaged to block additional Al vapor flux from reaching the samples and the current was ramped down to 0 A. Nitrogen was introduced into the chamber after 15 min to allow the samples to cool.

2.1.2 Deposition of chiral STF

After the low-pressure chamber was brought back to 1 atm pressure, the chamber door was opened and the tungsten-wire basket was replaced with a notched boat (S4-.005W, R.D. Mathis) which was filled with LaF_3 powder. Lanthanum fluoride was chosen as the partnering dielectric material in this research because it is somewhat hygroscopic, has a bulk refractive index slightly below that of SF11 glass, and has been shown to successfully facilitate the excitation of multiple SPP-wave modes for optical sensing of water-borne analytes [18]. Only two substrates, each with a 30-nm-thick Al thin film, were affixed to the sample holder. The other substrates were placed in a desiccator for future LaF_3 depositions. The bulk density, z -ratio, and tooling factor for LaF_3 were programmed into the deposition controller. The substrate holder was oriented to ensure that $\chi_v = 15^\circ$.

A computer-controlled stepper motor was programmed to rotate the sample holder about a central normal axis passing through it in increments of 18° with a 48-s pause between successive increments. Twenty 18° -steps were needed to complete the deposition of one structural period of thickness $2\Omega = 430 \text{ nm}$. The number N of structural periods was chosen to be either three or four, in order to later distinguish between SPP-wave modes and waveguide modes through optical experiments [18,29,30]. The shutter between the boat and the sample holder was engaged, the chamber door was closed, and the chamber was pumped to $P_{\text{base}} = 5 \times 10^{-6}$ Torr.

Current through the notched boat was increased in increments of 5 A until a suitable vapor flux was generated at about 95 A. Then, the shutter was disengaged and the collimated vapor flux was allowed to reach the samples. The deposition rate was held fixed at 0.4 nm s^{-1} with a $\pm 0.02 \text{ nm s}^{-1}$ variation, using the QCM. The shutter was re-engaged to block additional vapor flux from reaching the samples when the QCM indicated that a chiral STF of thickness either 1290 nm ($N = 3$) or 1720 nm ($N = 4$) had been deposited.

The chips were allowed to cool for 2 h before the chamber was brought to 1 atm pressure by opening the door. Then, the SMPRI chips were removed from the chamber and placed in a desiccator for 24 h.

2.1.3 Deposition of chiral STF with a silver-nanoparticle layer

Two types of SMPRI chips containing a silver-nanoparticle layer were fabricated in order to determine the effects of that layer on SPP-wave modes. In chips of the first type, the silver-nanoparticle layer was deposited immediately after the deposition of the first structural period of a three-period chiral STF. In chips of the second type, the silver-nanoparticle layer was deposited immediately after the deposition of the second structural period of a three-period chiral STF.

In order to deposit the silver-nanoparticle layer, the deposition of the chiral STF was interrupted by pausing the computer-controlled stepper motor and engaging the shutter to block the vapor flux from reaching the samples. Care was taken so that the periodicity of the chiral STF was not interrupted. The chamber was exposed to 1 atm pressure after allowing the samples to cool for 2 h. Then, the notched boat which housed LaF_3 was replaced with a dimple-style boat (S8A-.005W, R.D. Mathis) with a small chunk of bulk silver. The deposition-control program was adequately modified to accommodate the deposition of silver. The chamber was closed and then brought to $P_{\text{base}} = 1.5 \times 10^{-5}$ Torr. Current through the dimple-styled boat was slowly increased to 70 A. The shutter was then disengaged, and a steady deposition of silver continued at a rate of 0.2 nm s^{-1} until the QCM indicated that a 5-nm-thick film comprising silver nanoislands [31] was deposited on tops of the tips of the nanohelices of the chiral STF. The shutter was then re-engaged, the current was brought down to 0 A, the chamber was cooled for 2 h, and the chamber door was opened. The deposition of the chiral STF was resumed thereafter.

Figure 2 is a cross-sectional image of an SMPRI chip containing a three-period chiral STF with the 5-nm-thick silver-nanoparticle layer deposited after the first period. Its measured thickness of 1340 nm compares favorably with the $430 \times 3 + 30 + 5 = 1325 \text{ nm}$ thickness that was planned for.

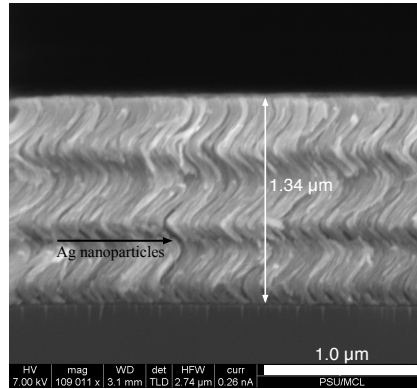


Fig. 2. Cross-sectional image of an SMPRI chip on a field-emission scanning electron microscope (FEI Nova NanoSEM 630, Hillsboro, OR, USA).

2.2 TKR measurements

For TKR measurements, an SMPRI chip comprising an Al film partnering an N -period-thick LaF_3 chiral STF with/without a silver-nanoparticle layer was positioned on the hypotenuse of a 45° - 90° - 45° prism made of SF11 glass (45-950, Edmund Optics, Barrington, NJ, USA), as shown in Fig. 3; thus, $n_{\text{prism}} = n_{\text{SF11}}$. The SF11 glass substrate of the chip was affixed to the

SF11 glass prism using a droplet of an index-matching liquid (1815X, Cargille Laboratories, Cedar Grove, NJ, USA), in order to remove any refractive-index mismatch and/or air bubbles while ensuring optical coupling between the substrate and the prism.

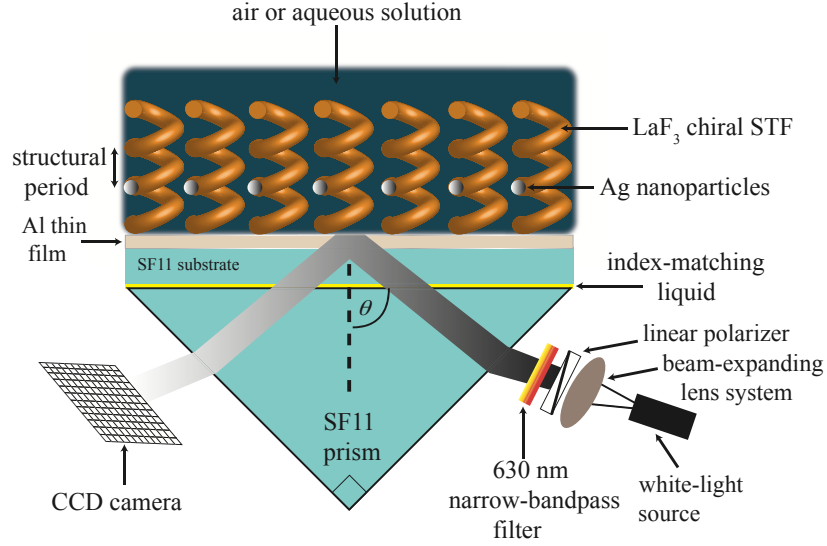


Fig. 3. Schematic of the TKR configuration wherein a substrate with an Al thin film partnering a LaF₃-chiral STF is affixed to the hypotenuse of an SF11 prism. A thin layer of silver particles is embedded after either the first (shown) or the second structural period in the chiral STF. A thin layer of an index-matching liquid is placed between the substrate and the prism. Light emitted from a white-light source passes through a beam-expanding lensing system, a polarizer, and a 630-nm narrow-bandpass filter before entering the prism through one of its two slanted faces. The intensity of light leaving the other slanted face of the prism is imaged with a CCD camera and recorded as a function of θ . Either air or an aqueous solution occupies the void regions of the silver-impregnated chiral STF.

The prism-chip assembly was then affixed to the vertex of a custom-built machine shown in Fig. 4 which measures the intensity of light exiting the second slanted face of the prism. This machine has one arm on which a fiber-optic cable (P1000-2-VIS-NIR, Ocean Optics, Dunedin, FL, USA) is mounted. The cable transmits light from a white-light source (HL-2000, Ocean Optics, Dunedin, FL, USA) into a beam-expanding lensing system, a linear polarizer (LPNIRE100-B, ThorLabs, Newton, NJ, USA), and a 630-nm narrow-bandpass filter (FB630-10, ThorLabs) towards one slanted face of the prism. The light exiting the polarizer can be chosen to be either *p* or *s* polarized. The intensity of light exiting the second slanted face of the prism is measured by a CCD camera (DCU223M, ThorLabs) mounted on the second arm of the machine. The two arms of the machine rotate in tandem as α is varied, the rotation being controlled using a stepper motor (NEMA23-597, Applied Motion Products, Watsonville, CA, USA) coupled with a 3540i stepper driver (3540i, Applied Motion Products), both operated using commercial software (SiNet Hub Programmer, Applied Motion Products).

The CCD camera captured the intensity of the reflected light in the form of a bitmap image using the uc480 Camera Manager (ThorLabs). In total, 250 images were captured for $\alpha \in [20^\circ, 70^\circ]$ at intervals of $\Delta\alpha = 0.2^\circ$. Although the stepper motor and the stepper driver are capable of delivering $\Delta\alpha = 0.007^\circ$, the associated software's limitations restricted the number of images that could be collected in a reasonable period of time. Each image was uploaded to an image-processing software ImageJ[®] (National Institutes of Health, Bethesda, MD, USA),

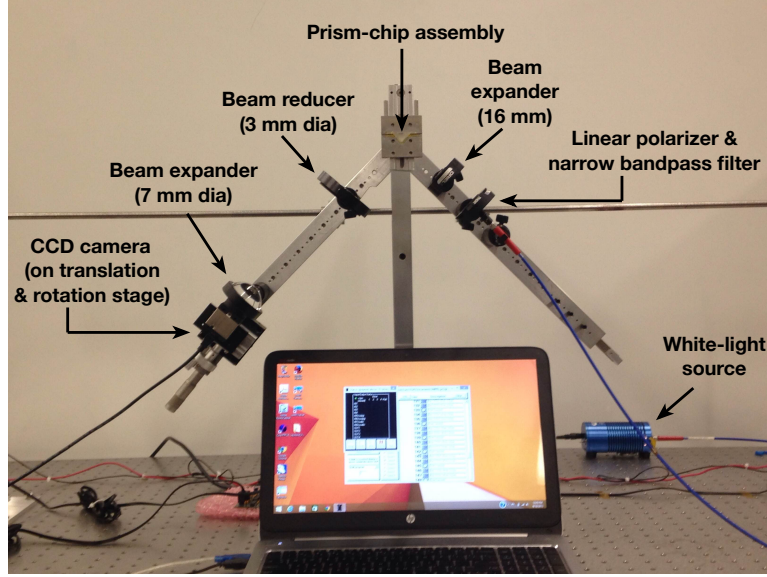


Fig. 4. Custom-built machine in which the prism-chip assembly is mounted in order to measure the normalized intensity R of light exiting the second slanted face of the prism as the angle θ is varied.

whereby the intensity of each image was calculated. The software does this by calculating the average grayscale-pixel intensity from 0 to 255 pixels when the user chooses a region of interest. The intensity of the reflected light was divided by that of the incident light to obtain the reflectance R as a function of θ . Either the void regions of the chiral STF were occupied by air or a drop of water or an aqueous solution was placed on the exposed surface of the chiral STF 20 min before the reflectance measurements were carried out.

3 RESULTS AND DISCUSSION

3.1 Air-filled void regions

3.1.1 Chiral STF without silver-nanoparticle layer

In Fig. 5a, R is plotted against $\theta \in (31^\circ, 59^\circ)$ for two SMPRI chips in which the void regions of the chiral STF are occupied by air and the incident light is p polarized. Whereas $N = 3$ for one chip, $N = 4$ for the other chip. In neither chip does the chiral STF have a silver-nanoparticle layer. No transmittance into air on the other side of the chiral STF is possible for $\theta > \sin^{-1}(n_{air}/n_{SF11}) = 34.22^\circ$.

Reflectance dips for the three-periods-thick chiral STF are present at $\theta \in \{35.79^\circ, 41.50^\circ, 45.63^\circ\}$, and for the four-periods-thick chiral STF at $\theta \in \{36.11^\circ, 40.75^\circ, 44.41^\circ, 46.63^\circ\}$. Allowing for no more than a 1° difference between the angular locations of SPP-wave modes, because the angular locations do have a weak dependence with a threshold on the thickness of the partnering dielectric material [11, 32], we identified three distinct SPP-wave modes in Fig. 5a with ellipses. The dip located at $\theta = 44.41^\circ$ for the four-period-thick chiral STF is a waveguide mode [11, 18, 29, 30] which depends on the thickness of the chiral STF.

In Fig. 5b, R is plotted against θ for two SMPRI chips in each of which the void regions of the chiral STF are occupied by air and the incident light is s polarized. A black ellipse contains the dips located at $\theta = 38.62^\circ$ and $\theta = 38.76^\circ$ for the three- and four-periods-thick chiral STFs, respectively. The close proximity of these dips to one another indicates that the incident s -polarized light excited an SPP-wave mode [11, 15].

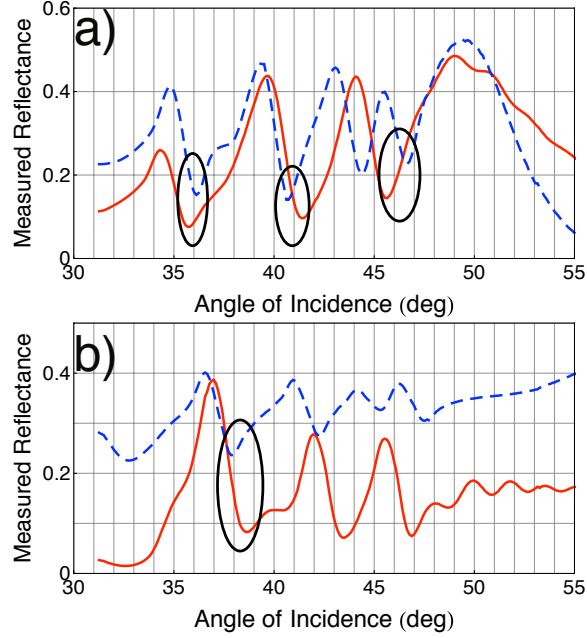


Fig. 5. R as a function of θ when the chiral STF in the SMPRI chip has either $N = 3$ (solid red lines) or $N = 4$ (dashed blue lines) periods and does not contain a silver-nanoparticle layer. The void regions of the chiral STF are occupied by air. The incident light is either (a) p or (b) s polarized. A black ellipse identifies the angular location of an excited SPP-wave mode.

3.1.2 Chiral STF with silver-nanoparticle layer

Figure 6a shows R as a function of θ when the incident light is p polarized, the chiral STF in the SMPRI chip has $N = 3$ periods, and the void regions of the chiral STF are occupied by air. Data are presented for the chiral STF without a silver-nanoparticle layer, the chiral STF having a silver-nanoparticle layer immediately after the first period, and the chiral STF having a silver-nanoparticle layer immediately after the second period.

Reflectance dips located at $\theta \in \{37.52^\circ, 42.84^\circ, 46.98^\circ\}$ when the chiral STF has a silver-nanoparticle layer immediately after the first period match well with the reflectance dips located at $\theta \in \{36.98^\circ, 42.96^\circ, 47.76^\circ\}$ when the chiral STF has a silver-nanoparticle layer immediately after the second period.

Comparison with the reflectance dips located at $\theta \in \{35.79^\circ, 41.50^\circ, 45.63^\circ\}$ (in Fig. 5a) when the chiral STF does not have a silver-nanoparticle layer indicates that this layer tends to shift the angular locations of the SPP-wave modes rightward on the θ axis. Concomitantly, this shift indicates that all three SPP-wave modes are mostly confined to within the first two or three periods of the chiral-STF/metal interface [32].

Figure 6b is the analog of Fig. 6a, but for incident s -polarized light. The reflectance dip located at $\theta = 39.94^\circ$ when the chiral STF has a silver-nanoparticle layer immediately after the first period matches well with the reflectance dip located at $\theta = 40.17^\circ$ when the chiral STF has a silver-nanoparticle layer immediately after the second period.

Comparison with the reflectance dip located at $\theta = 38.62^\circ$ (in Fig. 5b) when the chiral STF does not have a silver-nanoparticle layer confirms that this layer tends to shift the angular locations of the SPP-wave modes rightward on the θ axis. We concluded from Figs. 5 and 6 that the insertion of a silver-nanoparticle layer does not affect the location of the SPP-wave modes to an extent that would render the data uninterpretable.

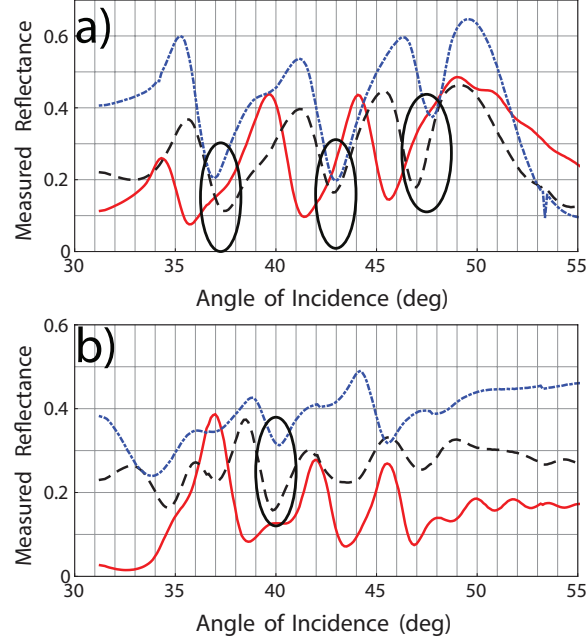


Fig. 6. R as a function of θ when the chiral STF has $N = 3$ periods, and its void regions are occupied by air. The incident light is either (a) p or (b) s polarized. Solid red lines: The chiral STF does not contain a silver-nanoparticle layer. Dashed black lines: The silver-nanoparticle layer is present after the first period in the chiral STF. Dot-dashed blue lines: The silver-nanoparticle layer is present after the second period in the chiral STF. A black ellipse identifies the angular location of an SPP-wave mode for the chiral STFs with a silver-nanoparticle layer.

3.2 Water-filled void regions

In order to confirm that the chiral STF containing a silver-nanoparticle layer can be used in an optical sensor, a water droplet was placed on top of the SMPRI chip, thereby filling the void regions of the chiral STF with water. No transmittance of light into water on top of the chiral STF is possible for $\theta > \sin^{-1}(n_{H_2O}/n_{SF11}) = 48.57^\circ$, where the refractive index of water $n_{H_2O} = 1.333$. Based on experience with chiral STFs without a silver-nanoparticle layer [18], we expected the number of SPP-wave modes to possibly decrease and their angular locations on the θ axis to shift rightward.

Figure 7a shows R as a function of θ when the incident light is p polarized, the chiral STF has $N = 3$ periods, and the void regions of the chiral STF are occupied by water. Data are presented for the chiral STF without a silver-nanoparticle layer, the chiral STF having a silver-nanoparticle layer immediately after the first period, and the chiral STF having a silver-nanoparticle layer immediately after the second period. Analogous data are presented in Fig. 7b for the incident light being s polarized.

In Fig. 7a, there are reflectance dips at

- (i) $\theta \in \{51.63^\circ, 54.76^\circ\}$ when the silver-nanoparticle layer is absent from the chiral STF,
- (ii) $\theta \in \{52.39^\circ, 55.82^\circ\}$ when the silver-nanoparticle layer is present immediately after the first period in the chiral STF, and
- (iii) $\theta \in \{51.52^\circ, 55.92^\circ\}$ when the silver-nanoparticle layer is present immediately after the second period in the chiral STF.

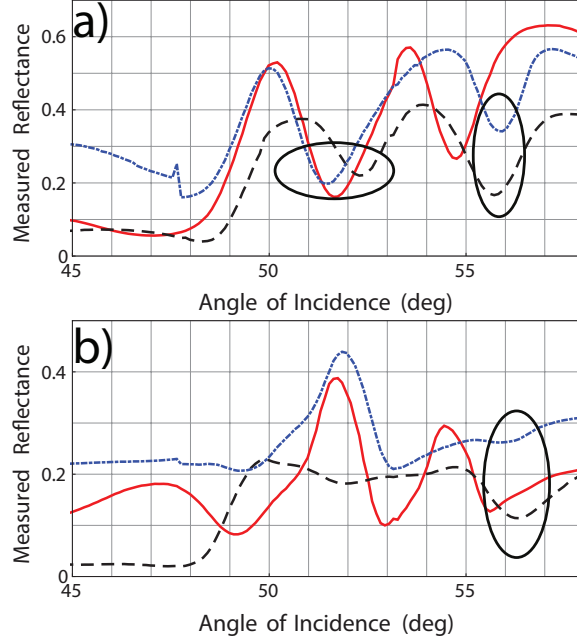


Fig. 7. Same as Fig. 6 but the the void regions of the chiral STF are occupied by water.

Thus, there are slight shifts of the angular locations of both SPP-wave modes due to the silver-nanoparticle layer, but the effect is not deleterious for either of the SPP-wave modes. Parenthetically, the reduction of the number of SPP-wave modes from three in Fig. 6a to two in Fig. 7a is due to the lessening of anisotropy and a tendency towards homogeneity when air is replaced by water in the void regions of a chiral STF [18].

Finally, in Fig. 7b, there are clear reflectance dips at $\theta = 52.93^\circ$ and $\theta = 55.64^\circ$ when the silver-nanoparticle layer is absent from the three-period-thick chiral STF. We think that only the dip at $\theta = 55.64^\circ$ possibly indicates the excitation of an SPP-wave mode, because only that dip is replicated (at somewhat higher values of θ) when the silver-nanoparticle layer is present both after the first ($\theta = 56.34^\circ$) and after the second ($\theta = 56.23^\circ$) periods of the chiral STF. However, as the last of those three dips is shallow, it may be of little use for sensing applications.

3.3 Sucrose-solution-filled void regions

Since the angular locations of an SPP-wave mode do not greatly depend whether the silver-nanoparticle layer is after either the first or second period in the SMRPI chip, we chose to limit further investigation to the silver-nanoparticle layer inserted after the first period of the chiral STF. Instead of water, we used droplets of 100, 200, or 300-mM aqueous solutions of sucrose [27]. The refractive indexes of those sucrose solutions are n_{100} , n_{200} , and $n_{300} \sim 1.338$, 1.343, and 1.348, respectively [33].

In Fig. 8a, there are reflectance dips at

- (i) $\theta \in \{51.63^\circ, 54.76^\circ\}$ when water infiltrates the void regions of the chiral STF,
- (ii) $\theta \in \{52.39^\circ, 55.39^\circ\}$ when a 100-mM-sucrose solution infiltrates the void regions of the chiral STF,
- (iii) $\theta \in \{52.70^\circ, 55.71^\circ\}$ when a 200-mM-sucrose solution infiltrates the void regions of the chiral STF, and

- (iii) $\theta \in \{53.37^\circ, 55.92^\circ\}$ when a 300-mM-sucrose solution infiltrates the void regions of the chiral STF,

when the incident light is p polarized. A silver layer is absent from the chiral STF. SPP-wave modes identified in the figure are labeled as '1' for the first group and '2' for the second group. The angular locations of the SPP-wave modes expectedly shift to higher values of θ as the refractive index of the infiltrating aqueous solution increases [18].

In Fig. 8b, incident s -polarized light excites SPP-wave modes in the vicinity of $\theta = 53^\circ$ and 55° . Though reflectance dips are clearly expressed, they are shallow. However, a trend which shows an increase in the angular location as the refractive index of the infiltrant fluid increases is evident, but the use of s -polarized incident light will require better selections of the chiral-STF material, the period 2Ω , and the number of periods N for optical-sensing purposes.

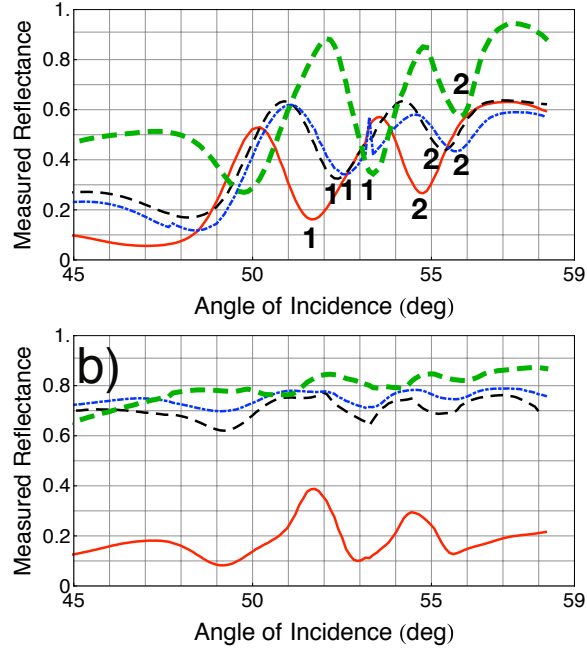


Fig. 8. R as a function of θ when the chiral STF in the SMPRI chip has $N = 3$ periods and does not contain a silver-nanoparticle layer. The void regions of the chiral STF are occupied by either water (solid red lines), 100-mM-sucrose solution (dashed black lines), 200-mM-sucrose solution (dot-dashed blue lines), or 300-mM-sucrose solution (long-dashed green lines). The incident light is either (a) p or (b) s polarized.

In Fig. 9, data are provided when the chiral STF contains a silver-nanoparticle layer after the first period. There are reflectance dips in Fig 9a at

- (i) $\theta \in \{52.28^\circ, 55.71^\circ\}$ when water infiltrates the void regions of the chiral STF,
- (ii) $\theta \in \{53.69^\circ, 56.34^\circ\}$ when a 100-mM-sucrose solution infiltrates the void regions of the chiral STF,
- (iii) $\theta \in \{54.01^\circ, 56.55^\circ\}$ when a 200-mM-sucrose solution infiltrates the void regions of the chiral STF, and
- (iii) $\theta \in \{54.76^\circ, 58.09^\circ\}$ when a 300-mM-sucrose solution infiltrates the void regions of the chiral STF,

when the incident light is p polarized in Fig 7a. The reflectance dip located at $\theta = 58.09^\circ$ when a 300-mM-sucrose solution infiltrates the void regions is evident yet highlights the limited range of θ accessible in our measurement apparatus. Comparison to Fig. 8a indicates that the angular locations of the SPP-wave modes shift slightly to higher values of θ when the silver-nanoparticle layer is present.

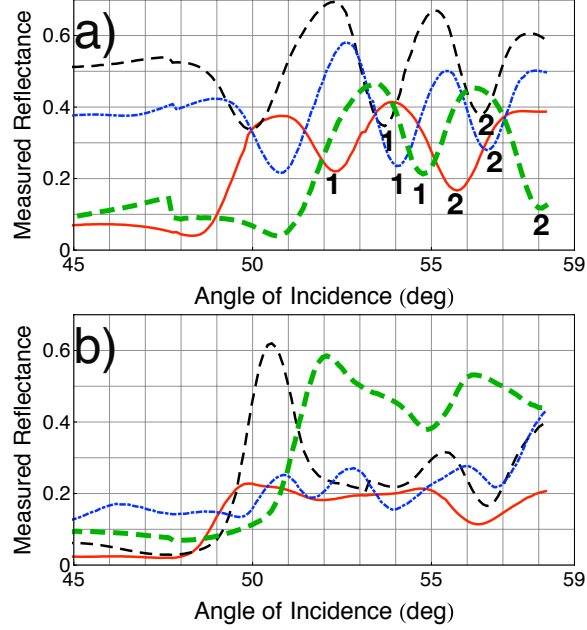


Fig. 9. Same as Fig. 8 but the chiral STF contains a silver-nanoparticle layer after the first period.

Figure 9b is similar to Fig. 9a, except that the incident plane wave is s polarized. Reflectance dips are clearly expressed but are shallow, similarly to those in Fig. 8b. Better selections of the chiral-STF material, 2Ω , and N appear necessary before s -polarized incidence could be used for optical sensing with the SMPRI chips.

3.4 Sensitivity

The sensitivity was calculated in order to estimate the fabricated SMPRI chip's capabilities as follows. Let $\theta(n_{infil}, m)$ denote the angle of incidence for a reflectance dip indicating the excitation of the SPP-wave mode labeled $m \in [1, 2]$ in Fig. 6a, when n_{infil} is the refractive index of the infiltrant fluid (which could be air, water, or an aqueous solution of sucrose, in this section). Then, a sensitivity with respect to water as the reference fluid is defined as [18]

$$\rho(n_{infil}, m) = \frac{\theta(n_{infil}, m) - \theta(n_{H_2O}, m)}{n_{infil} - n_{H_2O}}. \quad (2)$$

The sensitivities displayed in Table 1 are for an SMPRI chip whose chiral STF does not contain a silver-nanoparticle layer, and were calculated using data from Fig. 8a. The highest sensitivity of 152 deg/RIU is significantly larger than those reported in our previous study [18] wherein the highest sensitivity of 93.33 deg/RIU was reached for similar chips without a silver-nanoparticle layer; the increase may be attributed to the replacement of a photodiode with a CCD camera to measure R . A reduction in sensitivity from SPP-wave mode '1' to '2' is due to the compression of the values of $\sin \theta$ as θ increases.

Table 1. Sensitivity ρ for the m^{th} SPP-wave mode calculated using the data in Fig. 8a. The SMPRI chip does not contain a silver-nanoparticle layer.

m	n_{infil} RIU	$\theta(n_{infil}, m)$ deg	$\theta(n_{infil}, m) - \theta(n_{H_2O}, m)$ deg	ρ deg/RIU
1	1.333	51.63	-	-
	1.338	52.39	0.76	152
	1.343	52.70	1.07	107
	1.348	53.37	1.74	116
2	1.333	54.76	-	-
	1.338	55.39	0.63	126
	1.343	55.71	0.95	95
	1.348	55.92	1.16	77.33

Table 2. Sensitivity ρ for the m^{th} SPP-wave mode calculated using the data in Fig. 9a. The SMPRI chip contains a silver-nanoparticle layer.

m	n_{infil} RIU	$\theta(n_{infil}, m)$ deg	$\theta(n_{infil}, m) - \theta(n_{H_2O}, m)$ deg	ρ deg/RIU
1	1.333	52.28	-	-
	1.338	53.69	1.41	282
	1.343	54.01	1.73	173
	1.348	54.76	2.48	165.33
2	1.333	55.71	-	-
	1.338	56.34	0.63	126
	1.343	56.55	0.84	84
	1.348	58.09	2.38	158.67

The sensitivities displayed in Table 2 are for an SMPRI chip whose chiral STF does contains a silver-nanoparticle layer after the first period, and were calculated using data from Fig. 9a. Incorporation of the silver-nanoparticle layer significantly increases the sensitivity, by as much as 85% for the SPP-wave mode ‘1’. The effect is not impressive for the SPP-wave mode ‘2’, but even so the silver-nanoparticle layer does not depress ρ .

4 CONCLUDING REMARKS

Previous experimental research with incident monochromatic p -polarized light has shown that the interface of a metal thin film and a chiral sculptured thin film can be employed in the Turbadar–Kretschmann–Raether prism-coupled configuration to sense the presence of an analyte in a liquid infiltrating the chiral STF, because of shifts in the angular locations of multiple SPP-wave modes [18]. This experimental work has thus validated theoretical expectations [17].

Metal nanoparticles are often functionalized to serve as binding sites for recognition molecules in order to sense specific analytes. Therefore, we decided to embed a layer of silver nanoparticles inside a chiral STF and experimentally evaluate its effect on TKR sensing. Accordingly, we fabricated several substrate/metal/chiral-STF/silver-nanoparticles/chiral-STF multilayers to serve as chips for surface multiplasmonic resonance imaging. Aluminum was chosen for the metal thin film and lanthanum fluoride for the chiral STF. Several experiments were conducted to determine the effects of the silver-nanoparticle layer, which was deposited immediately after either the first or the second period of a three-periods-thick chiral STF. Monochromatic light was used to excite the SPP-wave modes. The incident light was either p or s polarized, and the angle of incidence θ on the prism/metal interface layer was varied. The reflectance R was measured as a function of θ , to determine the excitation of SPP-wave modes.

The angular locations (on the θ axis) of the SPP-wave modes were found not to greatly depend on whether the silver-nanoparticle layer is deposited after the first or the second period of a three-periods-thick chiral STF. This positive result indicates that the silver-nanoparticle layer is not debilitating for sensing applications.

Using aqueous solutions of sucrose as infiltrant fluids, we determined that the angular locations of the SPP-wave modes shifted rightwards when the refractive index of the infiltrant fluid increased. The use of a CCD camera for SMPRI was found to increase the sensitivity, in contrast to previous research [18] in which a photodiode had been used to measure R . Finally, the silver-nanoparticle layer was also found to enhance the sensitivity, this finding being in consonance with experimental results on SPP-wave-based sensors that do not contain chiral STFs but with metallic nanoparticles dispersed in the fluid to be sensed [24, 35].

Acknowledgments

SES and AL are grateful to the Charles Godfrey Binder Endowment at the Pennsylvania State University for financial support for this research.

References

1. J. Homola (Ed.), *Surface Plasmon Resonance Based Sensors*, Springer, Heidelberg, Germany (2006).
2. P. Chavel *et al.*, “Surface plasmon resonance imaging instrumentation and data handling for biochips: review and perspectives,” *Proceedings of SPIE* **6254**(1), 62540M (2006), <http://dx.doi.org/10.1117/12.679920>.
3. C. T. Campbell and G. Kim, “SPR microscopy and its applications to high-throughput analyses of biomolecular binding events and their kinetics,” *Biomaterials* **28**(15), 2380–2392 (2007), <http://dx.doi.org/10.1016/j.biomaterials.2007.01.047>.
4. I. Abdulhalim, M. Zourob, and A. Lakhtakia, “Surface plasmon resonance for biosensing: a mini-review,” *Electromagnetics* **28**(3), 214–242 (2008), <http://dx.doi.org/10.1080/02726340801921650>.
5. I. A. Buryakov, T. I. Buryakov, and V. T. Matsaev, “Optical chemical sensors for the detection of explosives and associated substances,” *Journal of Analytical Chemistry* **69**(7), 616–631 (2014), <http://dx.doi.org/10.1016/j.optcom.2005.04.001>.
6. Y. Yanase *et al.*, “Surface plasmon resonance for cell-based clinical diagnosis,” *Sensors* **14**(3), 4948–4959 (2014), <http://dx.doi.org/10.3390/s140304948>.
7. A. Ahmed *et al.*, “Biosensors for whole-cell bacterial detection,” *Clinical Microbiology Reviews* **27**(3), 631–646 (2014).
8. T. Turbadar, “Complete absorption of light by thin films,” *Proceedings of the Physical Society* **73**(1), 40–44 (1959), <http://dx.doi.org/10.1088/0370-1328/73/1/307>.
9. A. Otto, “Excitation of nonradiative surface plasma waves in silver by the method of frustrated total reflection,” *Zeitschrift für Physik* **216**(4), 398–410 (1968), <http://dx.doi.org/10.1007/BF01391532>.
10. E. Kretschmann and H. Raether, “Radiative decay of nonradiative surface plasmons excited by light,” *Zeitschrift für Naturforschung A* **23**(12), 2135–2136 (1968), <http://dx.doi.org/10.1515/zna-1968-1247>.
11. J. A. Polo Jr., T. G. Mackay, and A. Lakhtakia, *Electromagnetic Surface Waves: A Modern Perspective*, Elsevier, Waltham, MA, USA (2013).
12. P. G. de Gennes and J. A. Prost, *The Physics of Liquid Crystals*, 2nd ed., Clarendon Press, Oxford, United Kingdom (1993).
13. A. Lakhtakia and R. Messier, *Sculptured Thin Films: Nanoengineered Morphology and Optics*, SPIE Press, Bellingham, WA, USA (2005).

14. Devender, D. P. Pulsifer, and A. Lakhtakia, "Multiple surface plasmon polariton waves," *Electronics Letters* **45**(22), 1137–1138 (2009), <http://dx.doi.org/10.1049/el.2009.2049>.
15. T. H. Gilani *et al.*, "Surface plasmon resonance due to the interface of a metal and a chiral sculptured thin film," *Optical Engineering* **49**(12), 120503 (2010), <http://dx.doi.org/0.1117/1.3525282>.
16. A. Lakhtakia, Y. J. Jen, and C. F. Lin, "Multiple trains of same-color surface plasmon-polaritons guided by the planar interface of a metal and a sculptured nematic thin film. Part III: Experimental evidence," *Journal of Nanophotonics* **3**(1), 033506 (2009), <http://dx.doi.org/10.1117/1.3249629>.
17. T. G. Mackay and A. Lakhtakia, "Modeling chiral sculptured thin films as platforms for surface-plasmonic-polaritonic optical sensing," *IEEE Sensors Journal* **12**(2), 273–280 (2012), <http://dx.doi.org/10.1109/JSEN.2010.2067448>.
18. S. E. Swiontek, D. P. Pulsifer, and A. Lakhtakia, "Optical sensing of analytes in aqueous solutions with a multiple surface-plasmon-polariton-wave platform," *Scientific Reports* **3**(1), 1409 (2013), <http://dx.doi.org/10.1049/el:19870762>.
19. E. Yeatman and E. A. Ash, "Surface plasmon microscopy," *Electronics Letters* **23**(20), 1091–1092 (1987), <http://dx.doi.org/10.1049/el:19870762>.
20. E. Yeatman and E. A. Ash, "Surface plasmon scanning microscopy," *Proceedings of SPIE* **897**(1), 100–107 (1987), <http://dx.doi.org/10.1117/12.944524>.
21. C. E. Jordan *et al.*, "Surface plasmon resonance imaging measurements of DNA hybridization adsorption and streptavidin/DNA multilayer formation at chemically modified gold surfaces," *Analytical Chemistry* **69**(24), 4939–4947 (1997), <http://dx.doi.org/10.1021/ac9709763>.
22. G. Steiner *et al.*, "Surface plasmon resonance imaging of microstructured monolayers," *Journal of Molecular Structure* **509**(1-3), 265–273 (1997), [http://dx.doi.org/10.1016/S0022-2860\(99\)00226-4](http://dx.doi.org/10.1016/S0022-2860(99)00226-4).
23. J. S. Yuk *et al.*, "Analysis of blood proteins on protein arrays with a spectral surface plasmon resonance biosensor," *Current Applied Physics* **7**(1), 102–107 (2007), <http://dx.doi.org/10.1016/j.cap.2006.02.006>.
24. K.-S. Lee and M. A. El-Sayed, "Gold and silver nanoparticles in sensing and imaging: Sensitivity of plasmon response to size, shape, and metal composition," *Journal of Physical Chemistry B* **110**(39), 19220–19225 (2006), <http://dx.doi.org/10.1021/jp062536y>.
25. B. Rothenhäusler and W. Knoll, "Surface-plasmon microscopy," *Nature* **332**(6165), 615–617 (1988), <http://dx.doi.org/10.1038/332615a0>.
26. F. Abbas *et al.*, "Enhancement of dynamic sensitivity of multiple surface-plasmonic-polaritonic sensor using silver nanoparticles," *Plasmonics*, at press (2016), <http://dx.doi.org/10.1007/s11468-015-0133-x>.
27. S. E. Swiontek and A. Lakhtakia, "Influence of silver-nanoparticle layer in a chiral sculptured thin film for surface-multiplasmonic sensing," *Proceedings of SPIE* **9558**(1), 95580P (2015), <http://dx.doi.org/10.1117/12.2185842>.
28. S. E. Swiontek, M. Faryad, and A. Lakhtakia, "Surface plasmonic polaritonic sensor using a dielectric columnar thin film," *Journal of Nanophotonics* **8**(1), 083986 (2014), <http://dx.doi.org/10.1117/1.JNP.8.083986>.
29. T. Khaleque and R. Magnusson, "Light management through guided-mode resonances in thin-film silicon solar cells," *Journal of Nanophotonics* **8**(1), 083995 (2014), <http://dx.doi.org/10.1117/1.JNP.8.083995>.
30. L. Liu *et al.*, "Experimental excitation of multiple surface-plasmon-polariton waves and waveguide modes in a one-dimensional photonic crystal atop a two-dimensional metal grating," *Journal of Nanophotonics* **9**(1), 093593 (2015), <http://dx.doi.org/10.1117/1.JNP.9.093593>.

31. D. L. Smith, Thin-film Deposition: Principles & Practice, McGraw–Hill, New York, NY, USA (1995).
32. A. Lakhtakia and J. A. Polo Jr., “Energy flux in a surface-plasmon-polariton wave bound to the planar interface of a metal and a structurally chiral material,” Journal of the Optical Society of America A **26**(7), 1696–1703 (2009), <http://dx.doi.org/10.1364/JOSAA.26.001696>.
33. F. L. Hart and H. J. Fisher, *Modern Food Analysis*, pp. 490–491, Springer, New York, NY, USA (1971).
34. N. Mehan *et al.*, “Surface plasmon resonance based refractive index sensor for liquids,” Indian Journal of Pure & Applied Physics **43**(11), 854–858 (2005), [http://nopr.niscair.res.in/bitstream/123456789/8898/1/IJPAP 43\(11\) 854-858.pdf](http://nopr.niscair.res.in/bitstream/123456789/8898/1/IJPAP%2043(11)%20854-858.pdf)
35. A. Li *et al.*, “Ultrahigh enhancement of electromagnetic fields by exciting localized with extended surface plasmons,” Journal of Physical Chemistry C **119**(33), 19382–19389 (2015), <http://dx.doi.org/10.1021/acs.jpcc.5b05830>.

Stephen E. Swiontek received his BS in physics from Lock Haven State University in 2010 and his MS in engineering science from the Pennsylvania State University in 2012. Currently a PhD student, he received an SPIE Optics & Photonics Education Scholarship in 2015. His research interests include sculptured thin films, surface multiplasmonics, and optical sensing of chemicals and biochemicals.

Akhlesh Lakhtakia is the Charles Godfrey Binder Professor of Engineering Science and Mechanics at the Pennsylvania State University. His current research interests include nanotechnology, bioreplication, forensic science, solar-energy harvesting, surface multiplasmonics, and metamaterials, mimics, and sculptured thin films. He is a Fellow of OSA, SPIE, IoP, AAAS, APS, and IEEE. He was the sole recipient of the 2010 SPIE Technical Achievement Award.

List of Figures

Figure 1. Schematic of the TKR configuration for optical sensing. A substrate with a metal thin film is affixed to the hypotenuse of a 45° - 90° - 45° prism. Ideally, the substrate and the prism have the same refractive index. On the other side of the metal film is an aqueous solution (or some other fluid) containing the analyte to be sensed. A monochromatic p -polarized plane wave is incident onto one slanted face of the prism and emerges from the other slanted face of the prism.

Figure 2. Cross-sectional image of an SMPRI chip on a field-emission scanning electron microscope (FEI Nova NanoSEM 630, Hillsboro, OR, USA).

Figure 3. Schematic of the TKR configuration wherein a substrate with an Al thin film partnering a LaF_3 -chiral STF is affixed to the hypotenuse of an SF11 prism. A thin layer of silver particles is embedded after either the first (shown) or the second structural period in the chiral STF. A thin layer of an index-matching liquid is placed between the substrate and the prism. Light emitted from a white-light source passes through a beam-expanding lensing system, a polarizer, and a 630-nm narrow-bandpass filter before entering the prism through one of its two slanted faces. The intensity of light leaving the other slanted face of the prism is imaged with a CCD camera and recorded as a function of θ . Either air or an aqueous solution occupies the void regions of the silver-impregnated chiral STF.

Figure 4. Custom-built machine in which the prism-chip assembly is mounted in order to measure the normalized intensity R of light exiting the second slanted face of the prism as the angle θ is varied.

Figure 5. R as a function of θ when the chiral STF in the SMPRI chip has either $N = 3$ (solid red lines) or $N = 4$ (dashed blue lines) periods and does not contain a silver-nanoparticle layer. The void regions of the chiral STF are occupied by air. The incident light is either (a) p or (b) s polarized. A black ellipse identifies the angular location of an excited SPP-wave mode.

Figure 6. R as a function of θ when the chiral STF has $N = 3$ periods, and its void regions are occupied by air. The incident light is either (a) p or (b) s polarized. Solid red lines: The chiral STF does not contain a silver-nanoparticle layer. Dashed black lines: The silver-nanoparticle layer is present after the first period in the chiral STF. Dot-dashed blue lines: The silver-nanoparticle layer is present after the second period in the chiral STF. A black ellipse identifies the angular location of an SPP-wave mode for the chiral STFs with a silver-nanoparticle layer.

Figure 7. Same as Fig. 6 but the void regions of the chiral STF are occupied by water.

Figure 8. R as a function of θ when the chiral STF in the SMPRI chip has $N = 3$ periods and does not contain a silver-nanoparticle layer. The void regions of the chiral STF are occupied by either water (solid red lines), 100-mM-sucrose solution (dashed black lines), 200-mM-sucrose solution (dot-dashed blue lines), or 300-mM-sucrose solution (long-dashed green lines). The incident light is either (a) p or (b) s polarized.

Figure 9. Same as Fig. 8 but the chiral STF contains a silver-nanoparticle layer after the first period.